Applied Materials Today 37 (2024) 102082

Contents lists available at ScienceDirect

Applied Materials Today

journal homepage: www.elsevier.com/locate/apmt

Stable and homogeneous SPION-infused Photo-Resins for 3D-printing magnetic hydrogels

Ali A. Mohammed [a,b,1,*], Keyu Yao [c,1], Ieva Ragaisyte [c], Dominic Crestani [a,d], Connor W. Myant [a], Alessandra Pinna [c,e,f,*]

[a] Dyson School of Design Engineering, Imperial College London, SW7 2AZ, London, UK
[b] School of Design, Royal College of Art, SW11 4AY, London, UK
[c] Department of Materials, Imperial College London, SW7 2AZ, London, UK
[d] Department of Chemical Engineering, Imperial College London, SW7 2AZ, London, UK
[e] The Francis Crick Institute, NW11 AT, London, UK
[f] School of Veterinary Medicine, Faculty of Health and Medical Sciences, University of Surrey, Guildford GU2 7XH, UK

ARTICLE INFO

Keywords:
Super paramagnetic iron oxide nanoparticles (SPION)
3D printing
Additive manufacturing
Magnetic hydrogels
VAT photopolymerization
Photo-resins

ABSTRACT

3D printing of magnetic stimuli hydrogels has shown promise in low-resolution extrusion printing but integrating superparamagnetic iron oxide nanoparticles (SPION) into water-based photo-resins has posed challenges. Rapid agglomeration and sedimentation of SPION in photo-resins require continuous mixing during printing, leading to uneven nanoparticle (NP) distribution and inconsistent magnetic actuation. Here, we optimise the use of citric acid (CA) and l-sodium ascorbate (LA) as capping agents on the SPION's surface, before trialling them with photo-resins. Ultimately, we present a two-step approach to overcome these limitations, enabling high-resolution SLA-based 3D printing of hydrogels. By employing CA in both SPION and photo-resin preparation, we achieve a highly stable mixture that requires no agitation during printing, resulting in magnetically responsive hydrogels. This methodology can be applied to various photo-resin formulations, ensuring uniform NP distribution and enabling the 3D printing of stimuli-responsive materials for applications in soft robotics, aquatic micro-swimmers, and soft actuators. The breakthrough in stable and homogenous SPION-infused photo-resins has broad implications for tissue engineering, drug delivery, and regenerative medicine, offering novel biocompatible materials with resistance to stress and deformation. This approach can be extended to other NP with poor dispersion in hydrogels, paving the way for advanced functional materials in diverse applications.

1. Introduction

3D printing is proving to play a vital role in the future of prototyping and manufacturing with novel innovations and applications being developed at a rapid rate. The capability to produce complex and customisable geometries, unattainable with conventional fabrication techniques, alongside expansive materials options have fuelled the widespread adoption [1–3]. Hydrogels, characterised as 3D crosslinked, hydrophilic polymer networks, have sustainable mechanical strength, water swellability and outstanding biocompatibility making them perfect candidates for biomedical applications [4]. Previous studies have shown that by incorporating functional nanoparticles into 3D printable resins, such as hydrogels, it is possible to produce advanced stimuli responsive materials. Superparamagnetic iron oxide nanoparticles (SPION), commonly referred to as both magnetite (Fe_3O_4) and maghemite (γ-Fe_2O_3), have garnered particular interest due to their biocompatibility and unique magnetic, electrical, chemical, and physical properties [5]. However, issues surrounding uniform dispersion may be hindering its wide-spread implementation in VAT-based 3D printing and industrial applications.

By doping nanoparticles into hydrogels, nanocomposite hydrogels have been extensively studied for their broad properties and applications. Examples such as cellulose nanocrystals (CNCs) hydrogels have been put forward for applications ranging biomedical, energy storage, food, cosmetic and construction due to their biocompatibility as well as tuneable surface chemistry and impressive mechanical properties [6–9].

* Corresponding authors.
E-mail addresses: ali.mohammed@imperial.ac.uk, ali.mohammed@rca.ac.uk (A.A. Mohammed), a.pinna@surrey.ac.uk (A. Pinna).
[1] Share first authorship

https://doi.org/10.1016/j.apmt.2024.102082
Received 23 October 2023; Received in revised form 12 January 2024; Accepted 20 January 2024
Available online 2 February 2024

For example, a study by Adhikari *et al.* showed that graphene oxide can be added to polyamine gel to form a functional hydrogel that works as a reusable catalyst [10]. More recently, both Luo *et al.* [11] and Valentin *et al.* [12] developed dual crosslinked hydrogels by incorporating ions into the systems, such as sulfonate-modified silica nanoparticles (SiO_2-SO_3−Na+) and Fe^{3+}. These networks utilize physical bonds between ions and polymer chains to improve mechanical properties by dissipating deformation energy or healing the system due to their reversible sacrificial nature. In another study by Mohammed *et al.* it was demonstrated that cerium oxide nanoparticles could be used a building block for biomaterials in tissue engineering for its auto-catalytic properties [13]. SPION are one of the more prevalent nanoparticles in present research for various stimuli responsive applications [14].

Among some of the many industrial applications, the utilisation of nanoparticle fillers has been proposed for the absorption of various contaminants from solvents, drinking water and other aqueous systems [15–17]. Whilst conductive filler materials have been introduced for 3D printable circuit boards [18,19] and battery technologies [20]. The use of nanocomposite structures such as nanoparticles for the purpose of 3D printing has most notably shown great promise in the biomedical industry with milli-scale robots with applications ranging medical imaging, hyperthermia therapy and drug delivery [11,14,21–23]. Both Cazin *et al.* [24] and Ko *et al.* [25] investigated approaches of implementing SPION in 3D printing matrices to produce self-healing constructs for drug delivery and tissue engineering scaffolds. Sun *et al.* harnessed the magnetic properties SPION to create arthropod-inspired millirobots with the ability to move, rotate, grab and release with potential surgical applications [26]. Further, Yun-Won Lee *et al.* used a direct laser writing (two-photon polymerization) system to develop a 3D printed size-controllable hydrogel magnetic microscrews and micro-rollers that are able to respond to changes in magnetic fields amongst other stimuli such as temperature, pH, and divalent cations [27]. Similarly, Zhou *et al.* optimised a circulating vat photopolymerization (CVP) system to load $SrFe_{12}O_{19}$ magnetic fillers with 30 % particle loading and high uniformity to fabricate magnetic soft millirobots (MSMRs) with accurate miniature 3D structures [28]. And later, Simińska-Stanny *et al.* looked to improve on the actuation performance in multi-material, ferrogel, biocompatible actuators [29], whilst Huang *et al.* used a combination of ferromagnetic microparticles and Fe_3O_4 nanoparticles to 3D print magnetically functional devise using a high resolution homemade μCLIP [30]. However, many of the examples given are almost universally through extrusion printing or through low volume VAT printers which presents limits in both material choice, print volume and resolution.

The novelty of these technologies is evident by the challenges and limitations in stimulation response time, actuation efficiency and process limitations [31]. Scaling up to wide-spread adoption requires consistent and reproducible stimuli responses which is predominantly a consequence of homogeneous dispersion of nanoparticles. Furthermore, for biomedical applications, homogeneous distribution of nanoparticles is vital for their interactions with biological tissue [32,33]. The primary obstacles to this are agglomeration, sedimentation, and uneven distribution mostly due to high surface to volume ratio and inherent hydrophobic nature of the nanoparticles. These issues are exacerbated with magnetic nanoparticles as their dipole-dipole interactions and the presence of external magnetic fields in processing and application environments come into play [34–36].

To tackle this challenge, most groups opt for a mixture of mechanical stirring and ultrasonic vibrations to breakup and homogenise the nanoparticles shortly before crosslinking. Nonetheless, sedimentation and agglomeration can still quickly set in, especially in less viscous resins, only persisting for longer printing times. Furthermore, ultrasonic vibrations can result in undesirable filler damage or unintended polymerisation. One method to enhance stability and homogeneity in nanoparticle mixtures is to through surface modification by means of capping the nanoparticles with polymers, small molecules, and surfactants. Previous studies have demonstrated how dextran [37,38], chitosan [39,40], polyethylene glycol [41,42] and amongst other polymers [43] can be effective stabilisers whist sometimes offering improved biocompatibility and physicochemical properties. Furthermore, through attachment of various ligands, can also offer additional surface functionalities. Unfortunately, long term instability persists leading to undesirable agglomeration primarily due to the detachment of long and high M_r polymer chains from the nanoparticle surface. Moreover, for long chain polymers, fine control over coating thickness is vital to ensure minimal shielding of paramagnetic fields from magnetic nanoparticles. Therefore, smaller organic molecules such as citric acid have been used to synthesize stable SPION colloidal solutions with comparatively more negative zeta potential than when uncapped [21,44,45]. Both ascorbic acid (vitamin C) [46,47] and oleic acid [48] have also been widely used for their biocompatibility and antioxidant properties and have shown to be great candidates for capping nanoparticles. Furthermore, oleic acid has anti-cancer and anti-inflammatory properties but at the cost of low-solubility and bioavailability.

The encapsulation of nanoparticles can either be produced in a single step or through two-step capping. Single step capping, which is identical to the first stage in two-step capping [49], takes place during or after the synthesis process and is sometimes favoured owing to its simplicity although at the cost of desired dispersion type and stability. In a previous study, we showed that the addition of citric acid to a SPION-infused photo-resin for VAT 3D printing creates localised capping around the nanoparticles, resulting in short-term homogenisation and dramatic improvements in distribution [34]. However, the photo-resin still required manual mixing every 5 layers to avoid clustered agglomeration. By introducing a secondary capping step, greater control over surface chemistry can be had, thus improving stability and dispersibility. However, the added variabilities in capping agents and the order and timing of steps can all affect the final stability and dispersion. Meaning that determining the optimal capping method for a specific application or nanoparticle can be a lengthy process of trial and error.

In this study, we aim to investigate the impact of capping SPION during the synthesis process and their distribution in photo-resins, and the addition of a second capping step whereby citric acid is added to the photo-resin to enhance localised capping and homogeneity. The primary focus will be on the homogeneous dispersion of the capped SPION in poly (ethylene glycol) diacrylate (PEGDA) with either acrylamide or acrylic acid photo-resins for 3D printing. The mechanical properties and magnetic stimuli response of resulting 3D-printed structures are evaluated. While previous studies have demonstrated the need for and benefits offered by nanoparticle capping, to our knowledge, none have yet demonstrated a detailed comparison between one and two-step capping, and none have demonstrated the impact of the capping on the superparamagnetic properties of SPION, particularly for 3D printing. Furthermore, while previous studies have focussed primarily on extrusion-based 3D printing of SPION, the implications of this study on VAT-based 3D printing resins could allow for higher resolution, more reproducible stimuli-responsive 3D printed structures within a broader range of material choices for applications like soft robotics, microswimmers, and actuators.

2. Materials and methods

2.1. Materials

Anhydrous iron (II) chloride (98 % purity), iron (II) chloride tetrahydrate (98 % purity), citric acid monohydrate (99 % purity) (M_w=210.14), (+)-sodium l-ascorbate (99 % purity) (M_w=198.11) were utilized to synthesize iron oxide nanoparticles. They were purchased from Sigma-Aldrich (Dorset, UK).

The photocurable hydrogel resin consisted of acrylic acid (AA, average M_w=72.06, purity≥ 99 %), poly (ethylene glycol) diacrylate (PEGDA) (M_w~700, purity ≥ 99 %), lithium phenyl-2,4,6- trimethyl

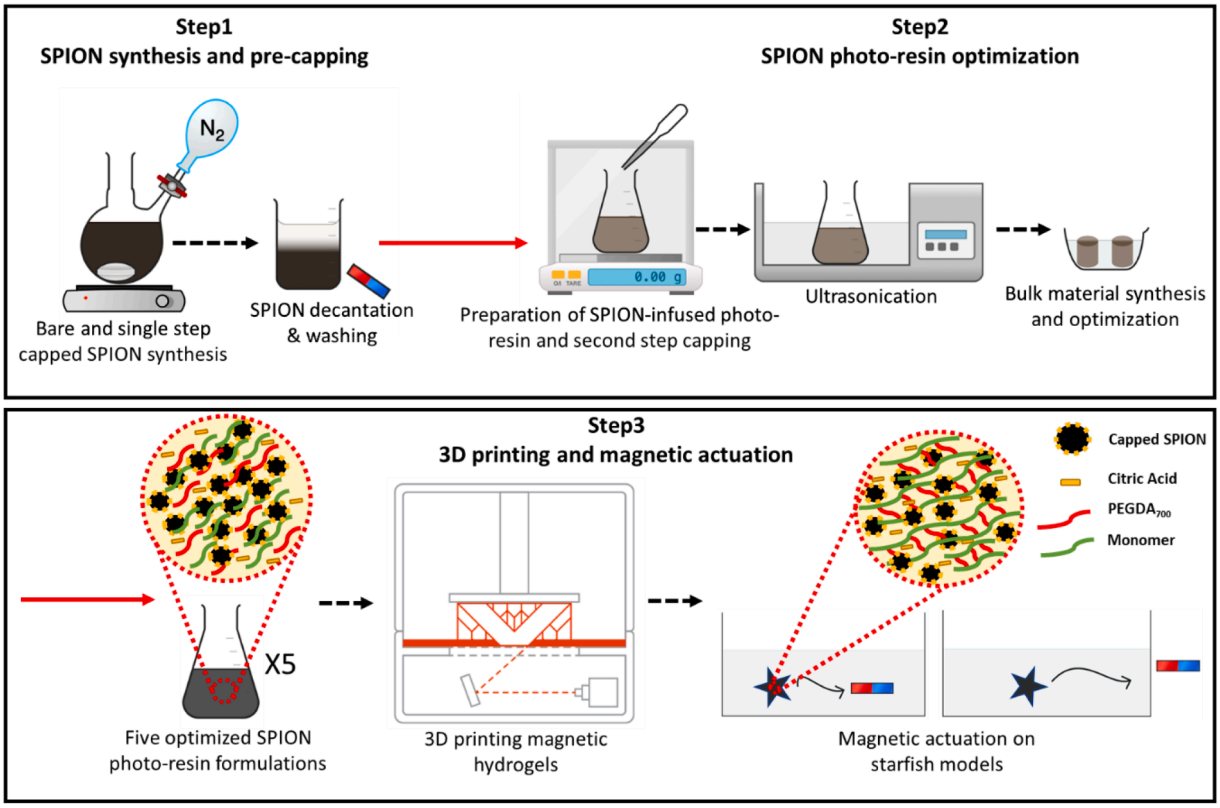

Fig. 1. Schematic showing the process of preparing the capped SPION (top), and 3D printing process (bottom) via stereolithography.

benzoyl phosphonate (LAP) (≥95%), which were also purchased from Sigma-Aldrich. Sodium hydroxide aqueous and hydrochloric acid aqueous solutions were diluted into 1 M solutions. Distilled water (DW) was obtained by ELGA@ DV25.

2.2. One-step synthesis of Bare and capped superparamagnetic iron oxide nanoparticles (SPION)

100 mL of NaOH (1 M) solution was added to a two-necked flask and placed on a hot plate whilst stirring at 650 rpm. High-purity argon (99.9 %) was pumped into the system to avoid potential oxidization of the SPION during synthesis. 3.25 g $FeCl_3$ and 2 g $FeCl_2{\bullet}4H_2O$ were measured and dissolved into a pre-prepared acidic solution (10 mL of HCl (1 M) in 50 mL DW), depicted in Fig. 1. This solution was then transferred drop wise into the alkaline solution and left for 45 min to allow precipitation and growth of the SPION. The SPION dispersion was washed five times via magnetic decantation with an N42 magnet, demonstrated in Figure S2. After each decantation, the impure solution was replaced with 50 mL of DW, and the resulting SPION were stored in argon degassed DW and labelled as Bare SPION. Four sets of reactions were then used for synthesis of the one-step capping using either citric acid monohydrate (CA) or (+)-sodium l-ascorbate (LA). Two concentrations for both capping agents were tested, 0.048 mol and 0.024 mol, referred to as high wt% and low wt%, respectively. The precipitation proceeded at room temperature for 5 min, and then the capping agents were added during the growth of SPION at 65 °C for 40 min. Samples were washed as described above and used for characterisation. The corresponding experimental details are recorded in the supplementary information Table S1.

2.3. Preparation of SPION-infused photo-resins with two-step capping for 3D printing

Photo-resins were prepared using SPION capped with either CA or LA. Initially, a series of base photo-resin consisting of crosslinker $PEGDA_{700}$, photoinitiator LAP and DW was prepared by measuring out associated masses into a clean beaker. Next, different combinations of acrylic acid, acrylamide, and polyacrylic acid were added to the base photo-resins. Finally, the capped SPION were added into the photo-resin and sonicated for 30 min. Table S3 summarises the optimized photo-resin formulations and the concentrations of capped SPION used in this work. For example, to prepare 50 g photoresin of AAm + 0.5wt% PAA: 8.5 g (17 wt%) AAm, 0.25 g (0.5 wt%) PAA, 3.75 g (7.5 wt%) $PEGDA_{700}$ and 37.5 g (75 wt%) DW were mixed into an amber container with a stirring bar and mixed. Next, based on the combined mass of AAm, PAA, $PEGDA_{700}$, 0.13 g (1%) LAP and 0.19 g (1.5%) High wt% CA capped SPIONs were added, mixed and sonicated in the photoresin. Finally, 500 μL CA (1 M) per 50 g of photoresin were added to the photoresin. The photo-resin was poured into a vat-tank and placed into a Formlabs Form2 SLA printer under 'Open Mode' using 'Clear resin' settings and 100 um layer height and spot size of 140 um. Two CAD models were uploaded, a cylinder with 1.3 cm diameter and 1.5 cm height, and a starfish with 2.3 cm diameter, using the software Preform, depicted in Fig. 1. After the print was complete, the hydrogels were removed from the build platform and post-cured in a water tank for 8 min using a Formlabs Form Cure to cure any unreacted compounds.

Characterisation methods can be found in the supplementary information (SI).

2.4. Nomenclature

SPION capped with citric acid (CA) or (+)-sodium l-ascorbate (LA) will be referred to as CA@SPION and LA@SPION, respectively. Additionally, they will also include a label indicating if high or low wt% of the capping agent was used e.g., CA@SPION (high wt% CA). All photo-resins contain $PEGDA_{700}$ in the base formulation; therefore, only the added monomers will be used for nomenclature i.e., a formulation containing acrylic acid (AA) and 1.0 wt% polyacrylic acid (PAA) will be

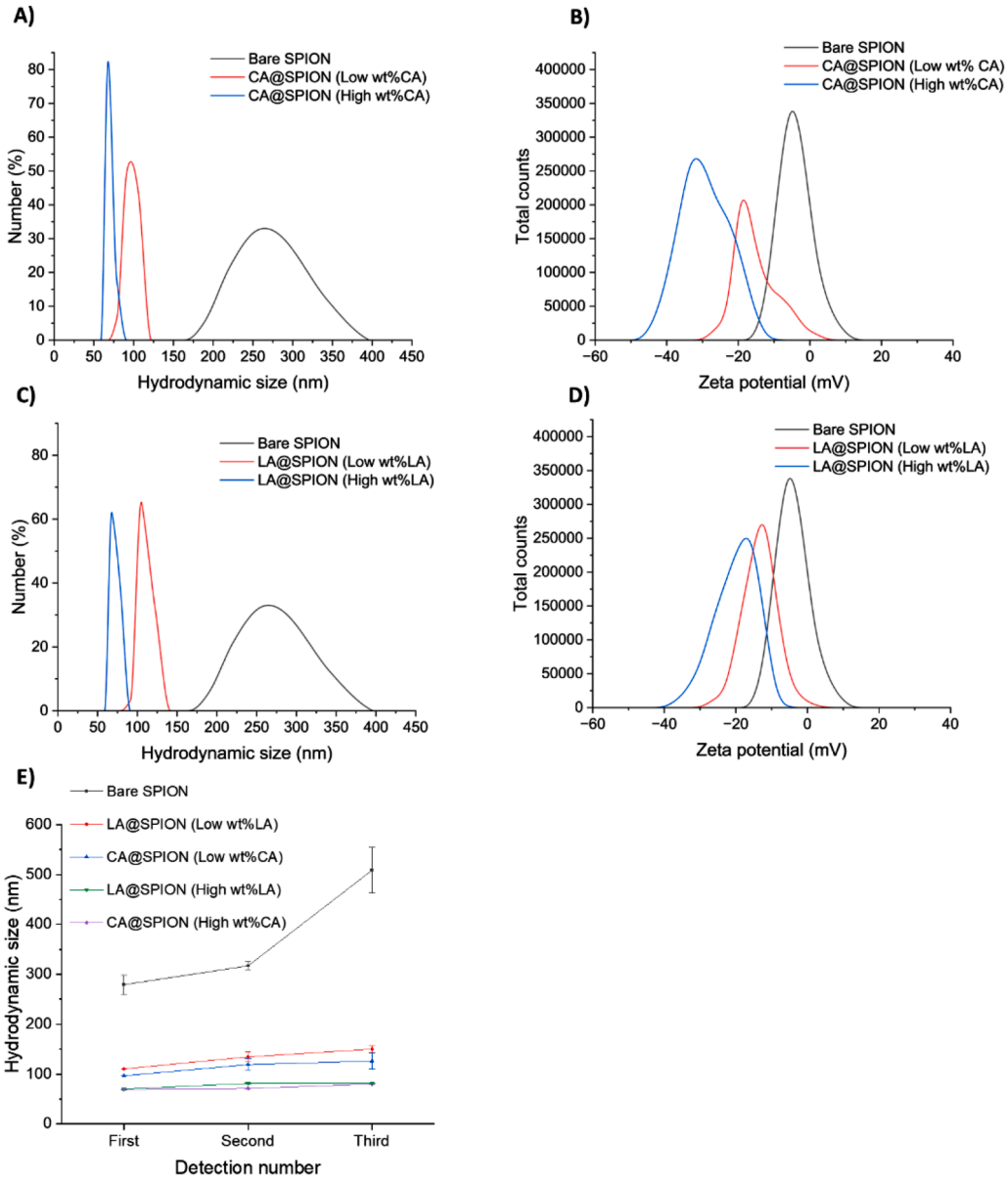

Fig. 2. Graphs showing (A) dynamic light scattering (DLS) of Bare SPION, citric acid (CA) capped SPION (CA@SPION) with a low wt% CA, CA@SPION with a high wt% CA; (B) Zeta potential of Bare SPIONs, CA@SPION with a low wt% CA, CA@SPION with a high wt% CA; (C) DLS of Bare SPION, sodium l-ascorbate (LA) capped SPION (LA@SPION) with a low wt% LA, LA@SPION with a high wt% LA; (D) Zeta potential of Bare SPION, LA@SPION with a low wt% LA, LA@SPION with a high wt% LA, (E) graph comparing the hydrodynamic size during three sequential dynamic light scattering (DLS) detections of Bare SPION, low and high wt% of CA@SPION, and low and high wt% LA@SPION.

Table 1
Summary of average hydrodynamic size, polydispersity index (PDI) and average zeta potential of the SPION samples after ultrasonication.

	Average hydrodynamic Size (nm)	PDI	Averaged Zeta Potential (mV)
Bare SPION	279 ± 19.1	0.77 ± 0.01	−10.0 ± 1.2
CA@SPION (High wt% CA)	69 ± 0.8	0.56 ± 0 0.01	−29.4 ± 3.9
CA@SPION (Low wt% CA)	97 ± 0.3	0.46 ± 0.02	−12.7 ± 2.3
LA@SPION (High wt% LA)	70 ± 2.8	0.56 ± 0.01	−19.3 ± 2.8
LA@SPION (Low wt% LA)	110 ± 0.2	0.54 ± 0.01	−12.5 ± 1.8

referred to as AA + 1.0 wt% PAA.

3. Results and discussion

3.1. SPION

Validation of SPION' stability and functionalized surface

FTIR spectroscopy was used to verify the successful capping on the surface of the SPION, spectra and discussion can be found in the SI (Figure S1).

The differences in hydrodynamic size (Fig. 2 (A, C)) and zeta potential (Fig. 2 (B, D)) of Bare vs capped SPION were characterized via DLS to verify the effect on monodispersity and colloidal stability through surface modification. The numerical results are summarised in Table 1. Bare SPION had an average hydrodynamic size of 279 ± 19 nm and a polydispersity index (PDI) of 0.77 ± 0.01, suggesting severe

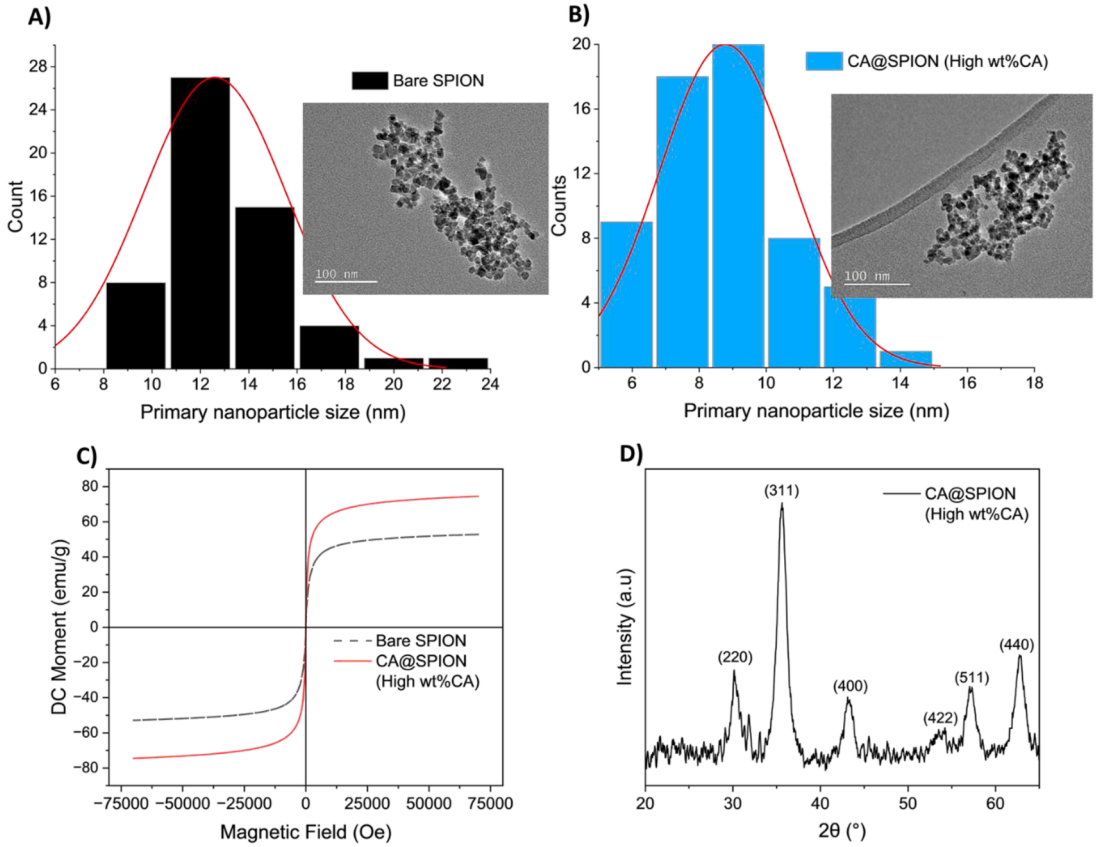

Fig. 3. (A) transmission electron microscope (TEM) image of Bare SPION and primary nanoparticle sizes calculated by averaging the diameter of 100 SPION using ImageJ software; (B) TEM image of CA@SPION with high wt% CA and primary nanoparticle sizes; (C) superconducting quantum interference device (SQUID) analysis of Bare SPIONs and CA@SPION with high wt% CA, and (D) X-ray diffraction (XRD) of CA@SPION with high wt% CA.

agglomeration with a high polydisperse state. However, the hydrodynamic size of the surface modified SPION decreased significantly and were proportional to the capping concentration i.e., a higher wt% of capping for both CA and LA resulted in smaller hydrodynamic sizes and lower PDI than low wt% capping. CA@SPION (high wt% CA) had the smallest hydrodynamic size and PDI. A decrease in the PDI values indicate that the capped SPION dispersions were able to maintain monodispersity.

The average zeta potential values aligned with the trends from DLS. The average zeta potential of the Bare SPION was -10.0 ± 1.2 mV. In contrast, CA@SPION (high wt% CA) exhibited both the smallest hydrodynamic size and most negative average zeta potential at 69.4 nm and -29.4 mV, respectively, indicating better colloidal stability than the Bare SPION and LA capped SPION. An image showing the impact of agglomeration and resulting sedimentation after 24 hr on Bare SPION compared CA@SPION (high wt% CA) can be found in the SI (Figure S3). The improved colloidal stability is due to the citrate ions on the surface of the SPION which can dissociate and bind via chemisorption with three carboxylate functional groups, thereby exposing negative charges and providing electrostatic and steric stabilization, which counteract van der Waals forces and hydrophobicity [50]. The result of this is a better stability in solution, and significant reduction in agglomeration and sedimentation.

Fig. 2 (E) shows the change in hydrodynamic size of each sample during three sequential detections. Values of each detection are summarised in the SI (Table S2). Bare SPION exhibited a fast agglomeration and increase in hydrodynamic size across each detection, suggesting a reduction in mono-dispersion and rapid agglomeration occur relatively fast resulting in poor colloidal stability. In contrast, the capped SPION were stable and did not exhibit significant changes in hydrodynamic size.

Investigation of SPION primary size, magnetic properties and phase composition

Fig. 3 (A-B) show TEM images of Bare SPIONs and CA@SPION (high wt% CA), with their corresponding primary nanoparticle size distributions ($n = 100$) calculated using ImageJ software. The CA@SPION (high wt%) had an average size of approximately 8.78 ± 1.99 nm, compared to 12.59 ± 2.93 nm for Bare SPION. This provides evidence that a one-step capping effectively synthesizes SPION with improved monodispersity with smaller diameters. This improvement is attributed to the citrate ions ability to anchor to the SPION surface, hindering the growth of the SPION nuclei after the nucleation [51]. Capping agents can drive preferential crystal growth in specific directions, impacting shape and size, with smaller diameters obtained with use of capping agents [52]. The capping process could render facets thermodynamically more favourable for crystal growth and therefore guide the shape and size of the SPION.

The magnetic properties of SPION, with and without CA capping (high wt% CA), were analysed using SQUID magnetometry at room temperature, and the magnetic profiles are presented in Fig. 3(C). Both magnetic curves display open hysteresis loops with negligible remanence and coercivity, indicating the superparamagnetic property of the single domain SPION with or without capping. The saturation magnetization (Ms) of the CA@SPION (high wt% CA) was approximately 74 emu/g, which is comparable to the values reported for previous polymer-coated Fe_3O_4 nanoparticles with P(NIPAAm-co-AEM) (73 emu/g) [50], and higher than previous studies on the citric acid capped SPION whose Ms values were below 60 emu/g [21,53,54]. The superparamagnetic behaviour and strong magnetic signal of the CA@SPION (high wt% CA) make it a promising candidate for use in nanocomposites

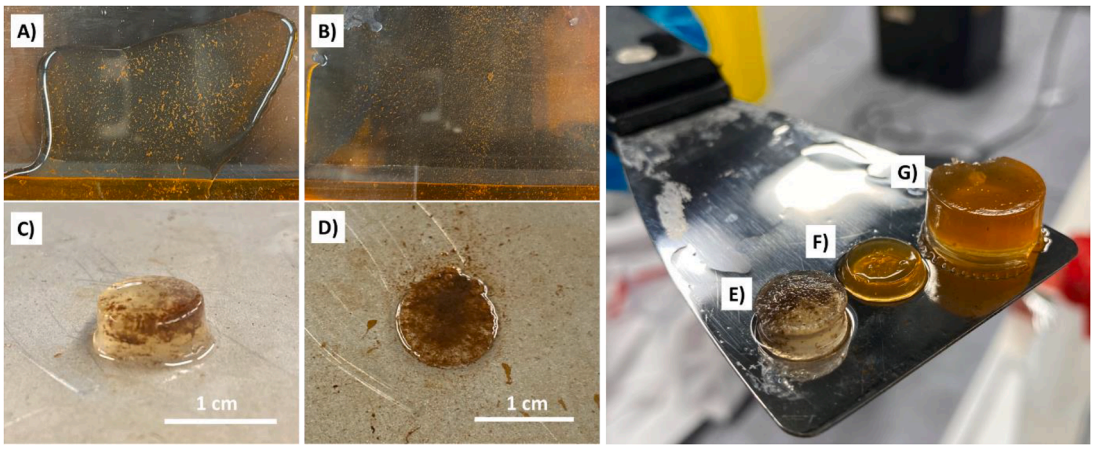

Fig. 4. Images showing (A) photo-resin with Bare SPION at the end of the print that were not manually mixed during the print to break up agglomeration; (B) photo-resin with one-step CA@SPION (low wt%) at the end of the print that were not manually mixed during the print to break up agglomeration; (C) hydrogel disc printed with Bare SPION without manual mixing of photo-resin during printing; (D) hydrogel printed with one-step CA@SPION (low wt% CA) without manual mixing of photo-resin during printing; (E) hydrogel printed with one-step LA@SPION (high wt% LA) without manual mixing of photo-resin during printing; (F) hydrogel printed with one-step CA@SPION (high wt% CA) without manual mixing of photo-resin during printing, and (G) hydrogel printed with one-step CA@SPION (high wt %) with manual mixing of photo-resin every 5 layers.

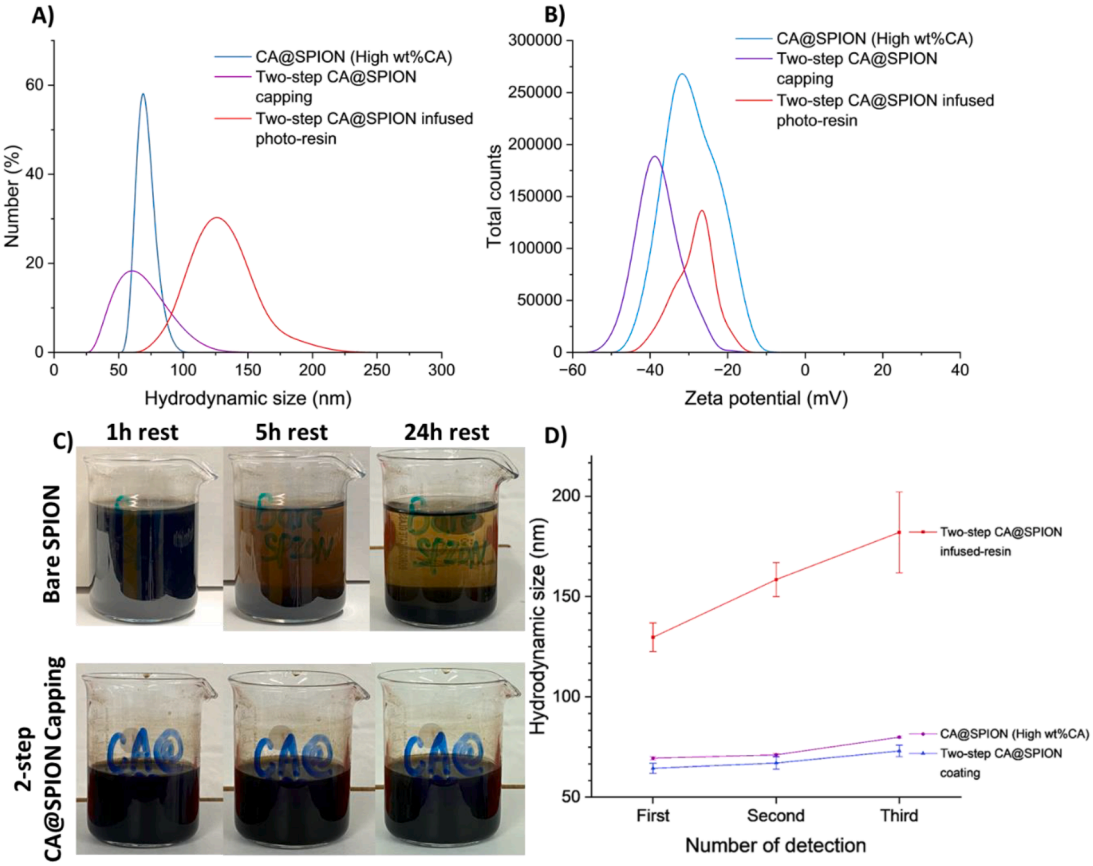

Fig. 5. Graphs showing (A) dynamic light scattering (DLS) and (B) Zeta potential of citric acid (CA) capped SPION (CA@SPION) with high wt% CA, two-step capped CA@SPION, and the SPION infused photo-resin using the two-step CA@SPION;(C) Images of Bare SPION vs. two-step capped CA@SPION at different time points (1, 5, 24 h); (D) The graph comparing the hydrodynamic size during three dynamic light scattering (DLS) detections of high wt% of citric acid (CA) capped SPION (CA@SPION), the two-step capped samples and corresponding SPION in the acidic photo-resin for SLA printing. Numerical values are provided in the SI Table S4.

and 3D printing. Notably, the saturation point of the capped SPION was higher than that of the Bare SPION (52.8 emu/g). Hossain S. *et al.* suggest that the citrate surface layer on the capped SPION effectively blocks surface oxidation, protecting the crystalline structure, and results in a higher Ms value [50]. The larger surface-to-volume ratio at a smaller nanoparticle size could also introduce more magnetic moments per unit volume [50,55]. However, other works have suggested that a reduced saturation magnetization might also occur [54,56], attributing to the formation of more surface dead layers of poorer crystallinity and surface spin disorder, leading to a decrease in the effective magnetic anisotropy

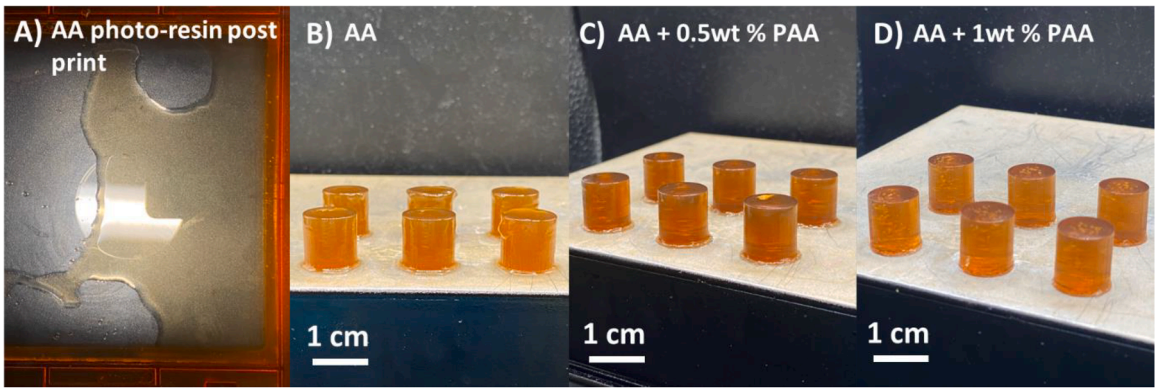

Fig. 6. Images showing (A) resin tank post print showing two-step capped SPION infused photo-resin (AA with 0.5 wt% SPION) free from agglomeration or sedimentation; (B) AA with 0.5 wt% SPION; (C) AAm + 0.5 wt% PAA with 0.5 % SPION, and (D) AA + 1.0 wt% PAA with 0.5 wt% SPION.

and a lower Ms value.

The phase composition, as well as crystallite size, of the CA@SPION (high wt% CA) were studied using the X-Ray Diffractometer. Fig. 3(D) show well-defined characteristic peaks assigned to (220), (311), (400), (422), (511), and (440) planes, indicating the presence of spinel crystalline (Fe_3O_4) and/or the maghemite (γ-Fe_2O_3) phases. Magnetite tends to oxidize into maghemite, forming a core-shell structure of core magnetite and outer shell maghemite [57]; however, XRD has limitations in distinguishing between phases due to their similarity in crystalline structures. Using Scherrer's equation, a 10.2 nm SPION crystallite size was calculated. The obtained result is in accordance with the 8.78 ± 1.99 nm SPION size reported in the previous TEM analysis.

The stability of SPION in photo-resins and efficacy of a two-step capping method

Initially, one-step LA and CA capped SPION were used to create various photo-resins and used in a stereolithography (SLA) 3D printer to investigate their colloidal stability during printing. Initial tests were carried out suing photo-resins with acrylic acid and 0.5 wt% loading of Bare or capped SPION. The photo-resin with Bare SPION had severe agglomeration during the printing process (Fig. 4(A)), with a significant colour gradient in the print suggesting an inhomogeneous distribution of SPION in (Fig. 4(C)). The photo-resin with CA@SPION (low wt% CA) also experienced agglomeration during printing, as shown in Fig. 4(B). However, this was less severe relative to the photo-resin with Bare SPION and showed improved distribution in the print (Fig. 4(D)).

Figs. 5 (E, F) show the improvement in homogeneity in the print using the higher wt% capping of LA and CA, with high wt% CA showing a significant improvement. These results align with the hydrodynamic sizes and surface zeta potentials, that suggested CA@SPION (high wt% CA) would perform best. Fig. 4(G) shows a completed print with CA@SPION (high wt% CA) where the print was stopped every 10 layers to manually mix the photo-resin to break up any agglomerates, resulting in a more homogenous print. Ideally, manual mixing should be avoided to ensure the duration of the print is not prolonged and to have a truly stable mixture, therefore a two-step capping method was developed to improve SPION distribution in the photo-resin. [34]

The two-step capping method showed to effectively improve CA@SPION (high wt% CA) colloidal stability, as demonstrated by a significant decrease in the hydrodynamic size of the particles (64.4 ± 2.5 nm) Fig. 5(A) and a shift in the zeta potential to a highly negative value around −40.7 ± 3.2 mV Fig. 5(B) compared to the single-step capped CA@SPION (high wt% CA).

Fig. 5(A) shows the hydrodynamic size of SPION-infused photo-resin had an average size of approximately 123 ± 7 nm. The zeta potential values in Fig. 5(B) follow a similar trend: the initial negative zeta potential around −33.2 ± 1.3 mV became less negative with time. Results indicate that the stability of the SPION are likely to be degraded under an acidic environment caused by the acrylic acid monomers, since excess hydrogen ions in the acidic photo-resins tend to protonate the negative-surface-charged SPION and reduce their electrostatic interaction capability [58]. However, this improvement to the photo-resin showed a highly stable mono-disperse mixture over a 24-hour period, as shown in Fig. 5(C). Within 24 h, the Bare SPION sample underwent rapid sedimentation and separation without external interference, suggesting quick agglomeration as expected. The two-step capped SPION showed a much stronger steric repulsion due to their negative surface charges, allowing the SPION to remain stable and dispersed efficiently over 24-hours, and several weeks when stored. This indicates that the photo-resins can be produced and shelved for re-use in the future without need to resuspend the SPION, providing evidence of a highly effective dispersion method that can now be applied to VAT polymerisation of magnetic materials.

Fig. 5(D) shows the size of the two-step capped SPION in the photo-resin had a slight increase in hydrodynamic size over during a three-detection run, which settled at 168 ± 20 nm. The numerical data are summarised in SI Table S4. The Zeta values represent high negative charges on the surface of the particles, enabling electrostatic repulsion and ensuring improved stability in solution [59]. The hydrodynamic size distribution of the two-step capped CA@SPION did appear to increase along with the polydispersity index (0.53 ± 0.01) compared to single-step capping. This observation suggests the two-step capping method leads to an incomplete SPION surface capping due to the citrate ions steric interaction or weak chemisorption with the SPION core. However, the photo-resin does not agglomerate significantly and does not result in any visual sedimentation.

3.2. *SPION-infused photocurable resin formulation optimization*

A series of five photo-resin formulations were optimized and used to 3D print cylindrical hydrogels, with homogeneously distributed 0.5 wt% SPION. The 3D printed hydrogels were swollen and tested under mechanical compression to investigate their physical properties. The two-step method maintained homogeneous photo-resins after printing was completed, and no manual mixing was required during printing. Figs. 6 (A-D) show the photo-resin post-print and the resulting magnetic hydrogels with homogenously distributed SPION. The magnetic photo-resins using acrylic acid (extremely acidic pH=1.5) did not appear to have apparent agglomeration throughout the printing process. (Fig. 6(B, D)).

Physical evaluation

Figs. 7 (A, B) illustrate the CAD models for 3D printing the samples and an example of the AA + 1.0 wt% PAA printed hydrogels. The dimensions of the 3D printed hydrogel cylinders matched the CAD models dimensions in width and height. However, an average of 7 % of over-curing was witnessed in the first few layers of the prints. This is due to repeated exposure of the laser in the first few layers to ensure adhesion

Table 2
Comparison of mechanical properties and swelling properties between 3D printed hydrogel composites containing the five different resin formulations. The SPION concentrations were kept the same in each formulation at around 0.5 wt%. In overall, the systems based on acrylic acid with lower PEGDA content had better softness and flexibility, proved by deformation degree and young's modulus.

Sample Name	Max compressive strength (kPa)	Deformation under stress (%)	Swelling degree by mass (%)	Swelling degree by volume (%)
AA	110 ± 7	41.2 ± 1.6	22.4 ± 2.3	25.7 ± 2.0
AA + 0.5 wt% PAA	111 ± 12	42.7 ± 4.0	36.1 ± 9.5	18.9 ± 4.8
AA + 1.0 wt% PAA	134 ± 18	44.3 ± 2.8	91.3 ± 14.5	61.2 ± 2.2
AAm	496 ± 52	30.5 ± 2.1	22.9 ± 0.4	9.6 ± 2.9
AAm + 0.5 wt % PAA	376 ± 40	29.5 ± 0.5	24.6 ± 0.6	17.7 ± 3.0

to the build plate, resulting in overcuring around the circumference of the printed hydrogel. The minimum feature size achieved was approximately 550 μm for the starfish, this could be improved further through the addition of photoabsorbers to limit light penetration and hence resolution, if required for future work, however this was not the objective or focus of this study [6]. Recent work has shown that it is possible to 3D print non-hydrogel magnetic materials with sub 40 um resolution using a low volume μCLIP with 20 wt% solid loading of magnetic particles (mixtures of micro and nanoparticles) [30]. Zhoe *et al.* were able to print up to 30 w/w% solid loading of a combination of magnetic micro and nanoparticles using a circulating vat photopolymerization (CVP) platform to form soft non-hydrogel millirobots, however, the study achieved similar resolution to the work here through an SLA with a spot size of 130 μm [28].

Compression strength and strain data is summarised in Table 2. Fig. 7 (C) provides a comparison of the mechanical properties of the five hydrogel formulations. The deformation-load curves of other resin formulations are shown in SI Figure S6. The stress/strain curves shown in Fig. 7(D) provide evidence that the AA hydrogels exhibited reduced stiffness, with an average compression strength that is 78 % lower, and an average deformation strain of 36 % that is higher, than AAm hydrogels. This difference is attributed to the higher crosslinking density in AAm hydrogels due to a higher PEGDA content, resulting in a denser and more rigid hydrogel. In contrast, formulations with AA contain higher monomer concentrations (25.5 wt% AA) than those of acrylamide (17.5 wt% AAm), result in a more flexible polymer network, thereby exhibiting an improved ability to sustain higher deformation. Moreover, the addition of poly (acrylic acid) softened the acrylamide hydrogel composites by lowering the ultimate compressive strength from 496 kPa to 376 kPa, shown in Fig. 7(C). In comparison, previous work has shown that the compressive strength for 3D printed AAm/PEGDA ranges from 255 ± 35 kPa to 577 ± 96 kPa [34].

The 3D printed hydrogels were swollen for 72 h, and changes in mass and volume (Table 2) were recorded. The results shown in Fig. 7(E) demonstrate that hydrogels based on acrylic acid exhibited higher water uptake capacity than those based on acrylamide, with the water absorption capability increasing with the amount of poly (acrylic acid) in both systems. This can be attributed to the carboxyl groups attached to the polymer chains in acrylic acid and poly (acrylic acid), which induce

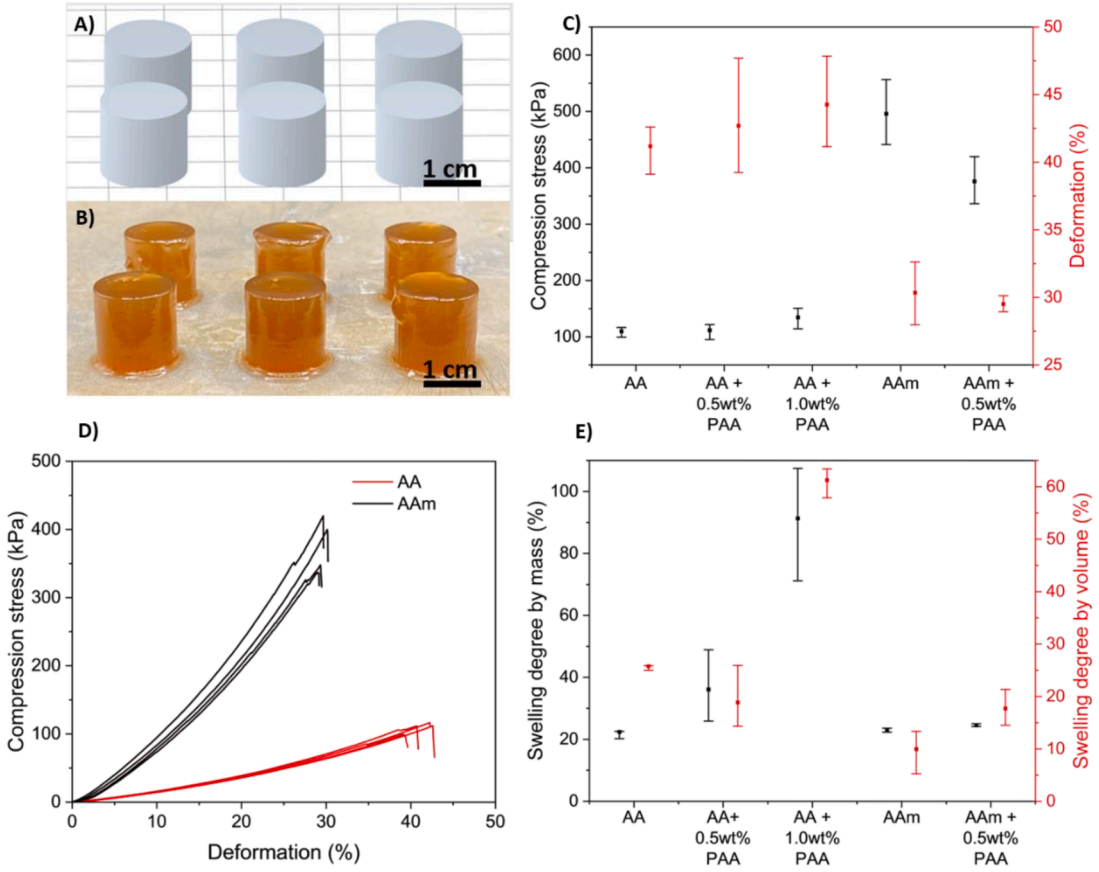

Fig. 7. (A) CAD models used for 3D printing SPION infused magnetic hydrogels; (B) 3D printed magnetic hydrogels using AA + 1.0 wt% PAA; (C) Compression curve for SPION infused photo-resins with acrylic acid (AA) and acrylamide (AAm) as the monomer. (D) graph comparing maximum compressive stress and deformation across all SPION infused photo-resins; (E) graph comparing swelling by mass (%) to swelling by volume (%) across all photo-resins.

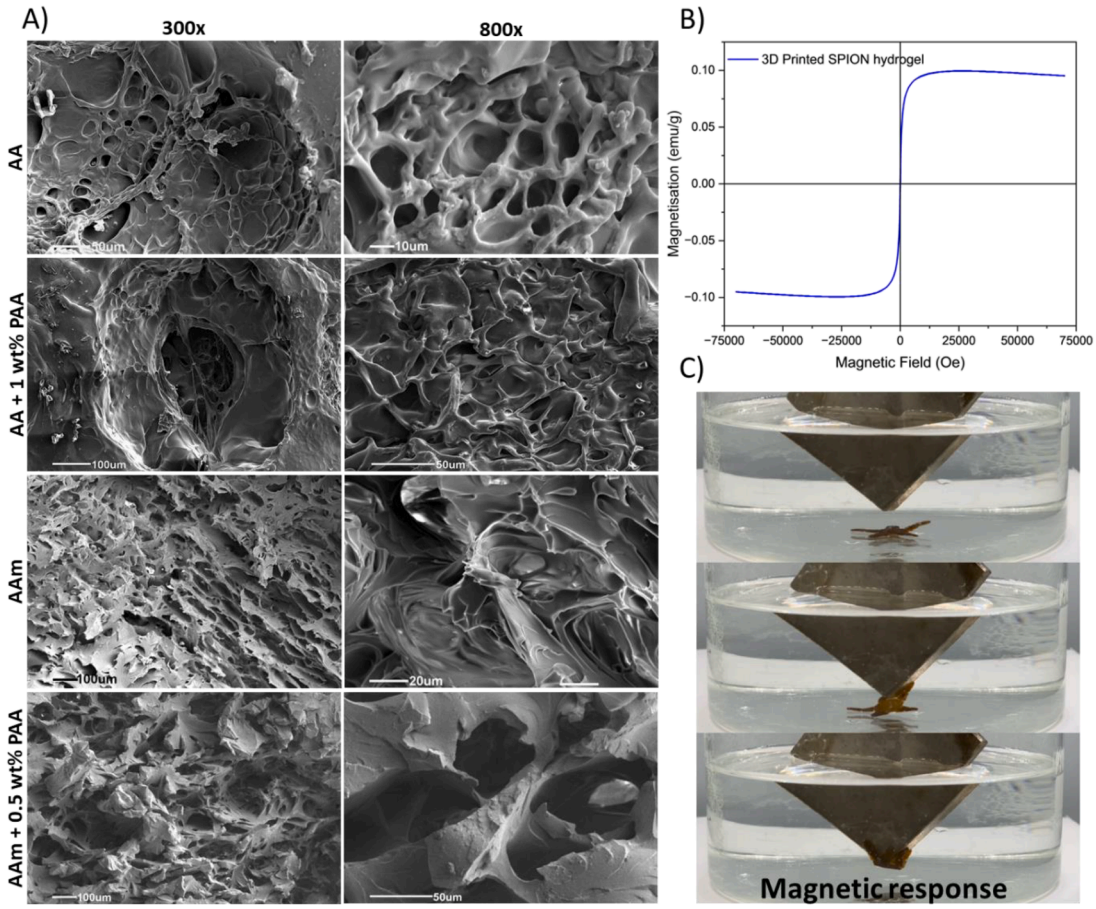

Fig. 8. (A) SEM images of 3D printed SPION infused hydrogels at different magnification, (B) Graph showing superparamagnetic magnetization profile of 3D printed AA + 1.0 wt% PAA hydrogels with 0.5 wt% SPION loading; (C) images of the vertical magnetic response of the 3D printed AA + 1.0 wt% PAA hydrogels with 0.5 wt% SPION loading in water.

electrostatic repulsion, especially in water, and promote volume expansion and swelling [60]. FTIR spectra and analysis of the hydrogels can be found in the SI (Figure S7).

SEM and Magnetic actuation

SEM images in Fig. 8(A) show a homogeneous porous network in the printed hydrogels, suggesting the high colloidal stability of the SPION did not impact the porous structure of the hydrogel and cause heterogeneity. Samples with AA exhibited less densely packed networks with well-dispersed porous structures relative to those with AAm. This variation could be attributed to the lower PEGDA content (1.5 wt%) in the AA system compared to the AAm photo-resins (7.5 wt%). A lower PEGDA content leads to a lower crosslinking density.

Fig. 8 (B) reports the magnetic hysteresis curve of a 3D printed hydrogel using two-step capped CA@SPION (high wt% CA) at 0.5 wt% in a hydrogel made of AA + 1.0 wt% PAA. The SPION-infused hydrogel maintained superparamagnetic properties with open hysteresis loops, negligible remanence and coercivity; however, the saturation magnetization significantly dropped to around 0.1 emu/g compared to CA@SPION (high wt% CA) that had a value of 74 emu/g. Therefore, the lower superparamagnetic behaviour of the SPION-infused hydrogel might be correlated to the capability of the polymer network to create a barrier around the SPION, hence reducing the magnetic performance of the SPION-infused hydrogel [15,16]. This follows a similar principle to core-shell structures, where modifications to the surface with nonmagnetic layers shield the magnetisation from the core [61]. Further, the reduced magnetisation is also attributed to the low SPION loading in the hydrogel of 0.5 wt% SPION loading was systematically increased from 0.5 wt% to 1.5 wt% to test the limits of the dispersion in the photo-resins, and to improve magnetic actuation, as demonstrated in the SI (Figure S7), and summarised in the SI Table S3. The photo-resins exhibited excellent colloidal stability throughout the printing process, providing evidence of the success and efficacy of the two-step capping mechanism. A saturation of 1.5 wt% loading of SPION was noted for all photo-resins, an increase above this value limited light penetration and caused light scattering, impacting the fidelity of the print [34]. To overcome this, the layer height was reduced from 100 μm to 25 μm which proved successful, as it allowed photopolymerization to occur closer to the limit of light penetration. Further studies will be required to assess higher loading concentrations of SPION at smaller build heights.

Starfish shaped hydrogels were 3D printed for all formulations to test in how they respond to magnetic stimuli in water. The results demonstrate the starfish arms' have a fast magnetic response and exhibit flexible movement, as shown in Fig. 8(C). Concentrations as low as 0.5 wt% loading of SPION showed to have good performance and response to magnetic stimuli, with loading at 1.5 wt% improving the speed and distance of the response. The starfish responded to vertical and horizontal magnetic stimuli and was able to firmly attach to the magnet. Once the magnet was removed, the starfish immediately sank and was able to restore its original shape. Videos of the starfish movement can be found in the SI (Video S1–5). Compared to previous works [16], here we show more flexible movement and faster actuating speeds, ascribing to the hydrogel's soft mechanical properties and lower solid-state density.

4. Conclusions

In conclusion, we show a novel two-step capping methodology that

can be used to create stable, homogenous, long-life photo-resins for 3D printing magnetic hydrogels. Our method involves a one-pot capping method using citric acid during the synthesis of the SPION, followed by a secondary capping step during photo-resin preparation. Our approach prevents sedimentation and agglomeration of SPION, an issue faced regularly in light-based 3D printing of nanocomposites in photo-resins of low viscosity, providing a uniform dispersion of SPION that maintain their superparamagnetic properties. These findings have broad implications for tissue engineering, drug delivery, and regenerative medicine, as well as soft robotics, where a range of different photopolymers can be used to achieve novel properties with biocompatibility and resistance to stress and deformation. Furthermore, our method may be applicable to other nanoparticles with poor dispersion in hydrogels, such as metallic and non-metallic nanoparticles. This opens avenues for designing advanced functional materials for various applications. In the study, we addressed limitations in magnetic-stimuli hydrogels by utilizing SPION as actuation fillers. Finally, a series of five finely optimized photocurable hydrogel composites containing acrylic acid or acrylamide for high-resolution 3D printing have been reported with high colloidal stability, eliminating manual mixing during printing. These new photo-resin formulation exhibited improved softness while maintaining flexibility post print and can be applied to a variety of applications that require movement in water such as micro-grabbers and micro-swimmers.

CRediT authorship contribution statement

Ali A. Mohammed: Conceptualization, Data curation, Formal analysis, Investigation, Methodology, Project administration, Resources, Software, Supervision, Validation, Visualization, Writing – original draft, Writing – review & editing. **Keyu Yao:** Data curation, Formal analysis, Methodology, Writing – original draft. **Ieva Ragaisyte:** Formal analysis, Methodology. **Dominic Crestani:** Methodology, Writing – original draft. **Connor W. Myant:** Resources, Validation. **Alessandra Pinna:** Conceptualization, Data curation, Formal analysis, Funding acquisition, Investigation, Methodology, Project administration, Resources, Software, Supervision, Validation, Visualization, Writing – original draft, Writing – review & editing.

Declaration of competing interest

The authors declare that they have no known competing financial interests or personal relationships that could have appeared to influence the work reported in this paper.

Data availability

Data will be made available on request.

Supplementary materials

Supplementary material associated with this article can be found, in the online version, at doi:10.1016/j.apmt.2024.102082.

References

[1] Y. Cheung, et al., Lab. Chip 7 (2007) 574.
[2] M. Stanton, et al., Lab. Chip (2015) 15.
[3] L.J. Tan, et al., Adv. Funct. Mater 30 (43) (2020) 2003062.
[4] E.M. Ahmed, J. Adv. Res. 6 (2) (2015) 105.
[5] A.V. Samrot, et al., Curr. Res. Green Sustain. Chem. 4 (2021) 100042.
[6] L.M. Kalossaka, et al., J. Mater. Res. 36 (21) (2021) 4249.
[7] K.J. De France, et al., Chem. Mater. 29 (11) (2017) 4609.
[8] D. Klemm, et al., Angew. Chemie Int. Edit. 50 (24) (2011) 5438.
[9] Y. Habibi, et al., Chem. Rev. 110 (6) (2010) 3479.
[10] B. Adhikari, et al., ACS Appl. Mater Interfaces 4 (10) (2012) 5472.
[11] F. Luo, et al., Adv. Mater. 27 (17) (2015) 2722.
[12] T. Valentin, et al., Polym. Chem. (2019) 10.
[13] A.A. Mohammed, et al., J. Mater. Chem. B 8 (14) (2020) 2834.
[14] S.M. Dadfar, et al., J. Nanobiotechnol. 18 (1) (2020) 22.
[15] E. Yan, et al., J. Phys. Chem. Solids 121 (2018) 102.
[16] D.P. Facchi, et al., Chem. Eng. J 337 (2018) 595.
[17] A.A. Edathil, et al., Int. J. Greenhouse Gas Control 83 (2019) 117.
[18] A. Joshi, et al., Chapter 3 - Polymer-based conductive composites for 3D and 4D printing of electrical circuits, in: K.K. Sadasivuni, et al. (Eds.), 3D and 4D Printing of Polymer Nanocomposite Materials, Elsevier, 2020, p. 45 (eds.).
[19] S.-C. Tsai, et al., Addit. Manuf. 51 (2022) 102590.
[20] P. Poizot, et al., Nature 407 (6803) (2000) 496.
[21] M.A. Dheyab, et al., Sci. Rep. 10 (1) (2020) 10793.
[22] W. Zhu, et al., Adv. Mater. 27 (30) (2015) 4411.
[23] J. Tang, et al., Extreme Mech. Lett. 46 (2021) 101305.
[24] I. Cazin, et al., RSC. Adv. 13 (26) (2023) 17536.
[25] E.S. Ko, et al., Carbohydr. Polym. 245 (2020) 116496.
[26] B. Sun, et al., Adv. Intell. Syst. 4 (1) (2022) 2100139.
[27] Y.-W. Lee, et al., ACS. Appl. Mater. Interfaces. 13 (11) (2021) 12759.
[28] Zhou, A., et al., (2022) 34 (15), 2200061.
[29] J. Simińska-Stanny, et al., Addit. Manuf. 49 (2022) 102506.
[30] Z. Huang, et al., Int. J. Extreme Manuf. 5 (3) (2023) 035501.
[31] F. Demoly, et al., Mater. Des. 212 (2021) 110193.
[32] N. Sadeghiani, et al., J. Magn. Magn. Mater. 289 (2005) 466.
[33] K. Quan, et al., ACS. Biomater. Sci. Eng. 6 (1) (2020) 205.
[34] A.A. Mohammed, et al., Heliyon. 9 (4) (2023) e14682.
[35] T. Vangijzegem, et al., Expert. Opin. Drug Deliv. 16 (1) (2019) 69.
[36] R. Cornell, U. Schwertmann, The Iron Oxides: Structure, Properties, Reactions, Occurrences and Uses, Wiley, 2003.
[37] A.K. Hauser, et al., Mater. Chem. Phys. 160 (2015) 177.
[38] Z. Shaterabadi, et al., Mater. Sci. Eng.: C 75 (2017) 947.
[39] S. Honary, et al., Int. Nano Lett. 3 (1) (2013) 48.
[40] P.B. Shete, et al., Appl. Surf. Sci. 288 (2014) 149.
[41] A. Mukhopadhyay, et al., ACS. Appl. Mater. Interfaces. 4 (1) (2012) 142.
[42] M. Yu, et al., Int. J. Mol. Sci. 13 (5) (2012) 5554.
[43] N. Zhu, et al., Nanomaterials. (Basel) 8 (10) (2018).
[44] A. Angheluta, et al., Revue Roumaine de Chimie 59 (2014) 151.
[45] J.-F. Lin, et al., J. Magn. Magn. Mater. 372 (2014) 147.
[46] V. Sreeja, et al., Appl. Nanosci. 5 (4) (2015) 435.
[47] O.S. Oluwafemi, et al., Colloids. Surf. B Biointerfaces. 79 (1) (2010) 126.
[48] T. Kuroiwa, Y. Higuchi, Polymers. (Basel) 14 (11) (2022) 2163.
[49] S. Laurent, et al., Chem. Rev. 108 (6) (2008) 2064.
[50] S. Hossain, et al., J. Mater. Res. 35 (18) (2020) 2441.
[51] A. Tari, et al., Physica B+ C 97 (1) (1979) 57.
[52] T.-H. Yang, et al., Angewandte Chemie Int. Edit. 59 (36) (2020) 15378.
[53] L. Li, et al., Microelectron. Eng. 110 (2013) 329.
[54] M. Arefi, et al., J. Iranian Chem. Soc. 16 (2019) 393.
[55] S. Ghosh, et al., Langmuir. 27 (13) (2011) 8036.
[56] K. Bakoglidis, et al., IEEE Trans. Magn. 48 (4) (2012) 1320.
[57] H. Sharifi Dehsari, et al., The J. Phys. Chem. C 122 (49) (2018) 28292.
[58] T. Granath, et al., Particl. Particle Syst. Characterizat. 39 (3) (2022) 2100279.
[59] Y. Sahoo, et al., J. Phys. Chem. B 109 (9) (2005) 3879.
[60] T.M. Valentin, et al., Polym. Chem. 10 (16) (2019) 2015.
[61] C. Wang, et al., Colloid. Surf. A: Physicochem. Eng. Aspect. 506 (2016) 393.